Interactive extraction of linear structures from LiDAR raw data for archaeomorphological structure prospection

Philippe Even, Axelle Grzesznik, Anne Gebhardt, Thomas Chenal, Philippe Even, Phuc Ngo

HAL Id: hal-03189641

https://hal.science/hal-03189641

Submitted on 4 Jul 2021

INTERACTIVE EXTRACTION OF LINEAR STRUCTURES FROM LIDAR RAW DATA FOR ARCHAEOMORPHOLOGICAL STRUCTURE PROSPECTION

Philippe Even[1,*], Axelle Grzesznik[2], Anne Gebhardt[3,4], Thomas Chenal[2], Pierre Even[5], Phuc Ngo[1]

[1] Université de Lorraine, CNRS, LORIA, Nancy, F-54000, France - (philippe.even, hoai-diem-phuc.ngo)@loria.fr
[2] CNRS UMR 6298 ARTEHIS, Besançon, F-25000, France
[3] Université de Strasbourg, CNRS, LIVE, Strasbourg, F-67000, France
[4] Université de Lorraine, CNRS, LIEC, Nancy, F-54000, France
[5] Université de Strasbourg, Strasbourg, F-67000, France

KEY WORDS: Airborne LiDAR, raw data processing, archaeology, geomorphology, forested area.

ABSTRACT:

A new detection and visualization tool to inspect raw LiDAR data for archaeological prospection is introduced in this paper. It allows the supervised extraction of linear structures (ridge or hollow) from the 3D ground points, for on-line detailed analysis of their cross and longitudinal profiles. Using raw data provides a richer information than an interpolated digital terrain model. In particular, the extraction process is made aware of point repartition irregularities caused by dense canopies in forested environments. The tool is based on a recent curvilinear structure extraction framework with fast execution time, that ensures a good interaction. Additional performance is achieved through the detection of the local terrain trend around the structure, that allows finer characterizations of the extracted structure. The suitability to several application purposes has been evaluated by archaeologists through real context experiments. The tool was first applied to the survey of a well-known medieval wall and to the identification of its less preserved parts, that are still undisclosed in the forested landscape. Then it was used in the scope of a prospective work about man impacts on its environment to detect and analyze old holloways and to get a better understanding of their local sunkness or the cause of their local deviations. Potential and limits of the tools are discussed. Open source and executable codes are left available for more extensive exploitation and possible integration into GIS softwares.

1. INTRODUCTION

Airborne laser scanning, also called LiDAR for Light Detection And Ranging, is a 3D data acquisition technique based on the emission of a laser beam swept over the measured scene and on the reception of echoes on hit obstacles. The measure of the signal travelling time provides a detailed survey of the overflight landscape (Wehr, Lohr, 1999). In forested environment, the received signal is composed of multiple echoes that correspond to the successive hit obstacles, from the forest canopy, down to lower vegetation levels and, finally, to the ground itself. A point classification is performed to separate ground points from low, medium, or high vegetation, and from other kind of specific features, such as water surfaces, buildings or wire lines. A surface is fit to ground points using optimization techniques to produce a digital terrain model (DTM) (Axelsson, 2000).

A LiDAR acquisition is of great help for archaeological prospection. The DTM provides a global view of the studied site surface. This is especially useful in forested areas, where terrain observations are largely hampered by a dense vegetation. Acurate bare soil visualizations can be obtained to detect surface details that may be missed during on-site prospections. Automatic tools to extract dedicated morphological structures are of great help to assist this heavy inspection task. However, the vegetation cover may also affect the laser beam penetration, producing holes in the ground point distribution, and large interpolations in the derived DTM. In particular, conifers are still a strong obstacle that impedes the laser beam reaching the soil (Amable et al., 2004, Devereux et al., 2005, Popescu et al., 2002). End users are not always aware of these

approximations when inspecting DTM visualizations, which may lead to many misinterpretations (Jones et al., 2007). DTM-based automatic processings may also be strongly affected by these aproximations.

This paper presents a new detection and visualization tool designed to inspect raw LiDAR data. It allows the supervised extraction of linear structures (ridge or hollow) directly from 3D surface point profiles, and a detailed analysis of their cross section along their run (see Figure 1). This tool implements a recent framework (Even, Ngo, 2020), refered to as the *extraction framework* in the following, relying on digital geometry algorithms to efficiently process raw ground points and get rid of DTM approximations. The performance of this framework was mostly evaluated on forest roads extraction, that is of minor interest for archaeologists. The scope here is to provide a better suited tool to specialist needs and to assess its effectiveness through experiments in real situation.
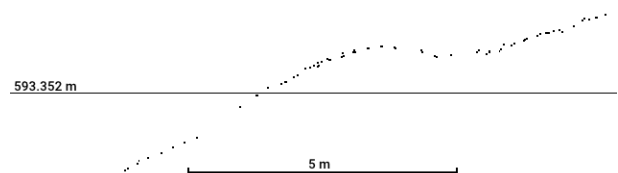

Figure 1. Example of wall (ridge) cross profile.

This work is done in collaboration with archaeologists, who are investigating the remains of man-made structures and their spatial organization. Suitability to archaeological prospection purposes has been evaluated by them through real context experiments. It was first used to extract and inspect well-known

---

* Corresponding author

archeological structures in order to test the new functionalities in comparison to more classical LiDAR use. The supervised detection performance was also tested on attempts to determine the extension of these structures in still unprospected areas where they become less prominent in the landscape. Then in the scope of an exploratory study, the tool was tested on the extraction and characterization of man-made linear hollow structures.

Some related works are briefly introduced in section 2. Section 3 describes the developed tool with a particular focus on new functionalities. Section 4 gives the main features of the used LiDAR data set. Section 5 presents achieved results on archaeological ridge structure extraction and analysis, while section 6 reports observed performance on hollow structure study. Finally, section 7 concludes this paper with a short discussion and opened perspectives.

2. RELATED WORKS

Airborne LiDAR is more and more commonly used for archaeological prospection tasks. In particular in forested areas, visual inspections of DTM views often reveal small morphological structures, that are occluded by the vegetation during field surveys (Devereux et al., 2005, Georges-Leroy et al., 2011). They can be delineated in the DTM and measured using geographical information system (GIS) post-processing (Sittler, 2004). A full-waveform LiDAR sensor may provide much better data (Doneus et al., 2008, Lasaponara et al., 2011). This technique registers a sampling of the complete laser signal rather than main echoes only. In forested areas, it provides a denser point cloud and better range determination (Mallet, Bretar, 2009), but at the price of a much larger amount of data storage and additional pre-processing steps. Moreover derived DTM interpolation errors still subsist. Dedicated visualization techniques to archaeological prospection have been developed and evaluated (Bennett et al., 2012, Challis et al., 2011, Mayoral et al., 2017, Štular et al., 2012), but none of them may highlight all the required morphological information at once, and most often, they are specifically selected according to application needs.

In complement of this manual inspection task, several studies have been led to automatically detect specific structures (Toumazet et al., 2017, Trier et al., 2015). They rely on well identified visual features to select relevant areas in the DTM, and on a geometric model of the structure, that provides a template to the recognition process. The recent development of efficient learning techniques based on support vector machines or on convolutional neural networks has contributed to the emergence of new detectors, that do not require the design of a dedicated model of the structure (Trier et al., 2016). They rather need a learning basis featuring a large set of annotated data, with as many different configurations as possible, to avoid learning bias. This condition is not always met in archaeology where most often, quite few artefacts are already identified. Moreover, annotation tasks may take a lot of time. The success rate is improved but still not perfect, and on-site surveys by specialists are still necessary to validate the results and complete the survey.

Most of automated or semi-automated archaeological structure detection tools rely on the DTM as it shows more practicable to use spatially arranged height values than sparse 3D points. A large set of pixel-based or object-based processing tools is now available (Sevara et al., 2016). But all these tools incorporate the interpolation errors. Direct processing of dense cloud of

3D points has also been studied. In particular, methods based on profile line analysis are usually effective and fast, but at our knowledge, most of them address structured environments, such as industrial scenes (Jiang, Bunke, 1994) or urban landscapes (Sithole, Vosselman, 2006), with more stable morphology and less surface perturbations than rural landscapes. Then, point density variations are much stronger in forested sites.

The goal of the present work is to develop a generic tool to extract linear structures from raw LiDAR data and to allow a detailed visualization of their cross and longitudinal profiles. In order to get rid of DTM interpolation errors, only raw ground points are processed. No attempt is made to interpret the found structures. This process is left under control of specialists. In counterpart, fast responses must be ensured to reach a sufficient interaction level. In lack of comparable method in literature and of available ground truth for evaluation, achieved experiments aim at assessing the tool effectiveness in real situation to support archaeomorphological studies.

3. ILSD: AN INTERACTIVE TOOL TO EXTRACT AND ANALYZE LINEAR STRUCTURES

Based on the extraction framework algorithms proposed in (Even, Ngo, 2020), a new tool called ILSD (for Interactive Linear Structure Detector), dedicated to archaeological prospection purposes, has been developed and is available as an open source software. It allows to extract and analyze linear structures (ridge or hollow) by detecting and tracking their cross profiles in the 3D ground point cloud of the LiDAR data set. A *ridge structure* corresponds to an elongated structure above the local terrain trend, for instance a wall or a dike, whereas a *hollow structure* extends similarly below the local trend, for instance a ditch or a trench. The detection process is left under control by the user, who decides where it should take place by manually drawing an initial stroke across relevant details on the DTM view. The result is immediately displayed for validation and more thorough analysis of the point profiles. To that end, two graphical views are displayed: the first one allows to inspect successive cross profiles of ground points all along the structure; the second provides the longitudinal curvilinear profile of ground points. They show the distribution of points used for the extraction, and may reveal useful details for interpretation by experts. Additionally, measures of the structure cross sections area may be computed and also integrated to give an estimation of the volume between manually selected bounds on the displayed layout.

Compared to the method of (Even, Ngo, 2020), the ridge model has been improved to better suit to the different archaeological or geomorphological structures addressed in this work and to provide more reliable geometric estimations. Moreover, the extraction of hollow structures has also been added. The principle of the extraction framework is just summarized in the following section. More details can be found in (Even, Ngo, 2020). The improved ridge model is then introduced in details. Finally main implementation features and source code access are given at the end of the section.

3.1 Sketch of the extraction framework

Preliminary, in order to speed up point collection operations, LiDAR ground points are arranged into a point grid $\mathcal{G}$ matching the DTM grid $\mathcal{I}$. In the following, we call *scan* a straight line segment of $\mathcal{I}$. Let $\vec{V}_S$ be the director vector of scan S.

From a scan S, corresponding points in $\mathcal{G}$ are collected, projected orthogonally to $\vec{V}_S$, and sorted along $\vec{V}_S$, to get a *profile* $\mathcal{P}$. Then, a model of the structure is fit to this profile. It provides a *model template* $\mathcal{M}$, defined as a set of geometrical values m^k (positions or dimensions) assigned to model parameters. The extraction framework is composed of three sequential steps, as illustrated in Figure 2:

1. initial recognition of the structure from an input scan,
2. extension on both sides of the input scan,
3. final validation and cleaning.

The input of step 1 is a stroke manually drawn on the DTM view, that provides a start scan $S_0(P_1 P_2)$ (see Figure 2, a), then a start profile $\mathcal{P}_0$ (see Figure 2, b), and a start template $\mathcal{M}_0$. In case of fail, this operation is repeated on near adjacent scans to get a reliable start profile, and definitely aborted if no occurance of the structure can be recognized in this area.

In case of success, step 2 consists in tracking the structure on both sides of the start scan S_0 as far a possible. It is an iterative process based on the analysis of successive adjacent scans S_i parallel to S_0 and centered on the position of the last valid template $\mathcal{M}_j$. Again, a new template $\mathcal{M}_i$ is obtained by fitting the model to the profile $\mathcal{P}_i$. For each template element m_i^k, if the difference $|m_i^k - m_j^k|$ exceeds a tolerance threshold Δm^k, then the profile is discarded. This condition enforces spatial consistency of the extracted structure. Threshold values Δm^k are left under user control to adapt to different types of structures. The extension stops after occurence of a predefined number of successive tracking fails. This parameter controls the crossing of local perturbations. Notice that local point lacks are not considered as local perturbations. In that specific case, the fail count is not incremented. This helps to cross occluded areas. A structure composed of a set of cross profiles is produced at the end of this step. DTM scans are piled up (left side) and down (right side) on the user interface for a quick visual control of the profiles (see Figure 2, c).
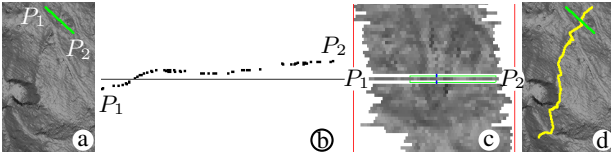

Figure 2. Extraction framework; a) input stroke $P_1 P_2$; b) first point profile P_0; c) set of scans S_i used on both sides; d) detected ridge based on accepted profiles.

In final step 3, a validation test checks if the structure contains a sufficient number of profiles, and the cleaning operation prunes disconnected profiles on both ends. The resulting structure is finally superimposed to the DTM view (see Figure 2, d).

Fast discrete geometry algorithms are used for adjacent scan selection and for model fitting operations. Several hundreds of meters long structures are detected in a fraction of a second on a standard computer. So the user can adjust his manual selection on the fly to get the best structure.

3.2 The new ridge model

The ridge structure is defined by a set of cross sections, called *bumps*. The bump lies on a straight baseline, and the area of the polygon closed by the bump surface points and the baseline can be measured. Additionally to the model proposed

in (Even, Ngo, 2020), the local terrain trend may be detected on both sides of the bump in order to get more accurate detection and measures, and the bump center is computed with more accuracy. Hollow structure detection is also implemented.

A trend is modelled as a set of adjacent profile points that hold inside a thick straight segment. Front trend $\mathcal{T}$ and back trend $\mathcal{T}'$ are searched on each side of the profile. Given a start point C_T, next profile points are inserted in the trend from the nearer to the further in both directions (see Figure 3). At each point insertion, the trend thickness is controlled to check that it does not exceed a given threshold ε. At iteration i of step 2, C_T is set to the nearest profile point to the center of last valid trend $\mathcal{T}_j$. At step 1, no prior position is available, then C_T is set to the first point of the profile to detect the initial front trend $\mathcal{T}_0$, and to the last point to get the initial back trend $\mathcal{T}_0'$; both trends extend from profile end towards the searched structure.
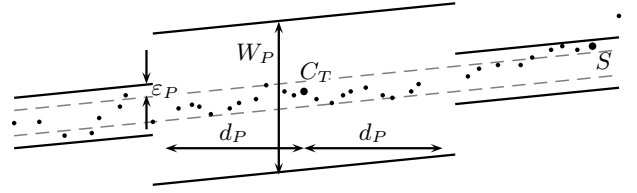

Figure 3. Trend pinching procedure (in step 2).

A pinching procedure is performed in both steps to get a more accurate detection of each trend area. The maximal thickess ε is initially set to a large value W_P. When reaching observation distance d_P to start point C_T, it is fit to the already detected trend thickness, dilated by a small safety margin ε_P to incorporate some possible terrain roughness. Passed this pinching operation, the trend cannot get thicker any more. The trend detection stops when the first point out of the thickness threshold is met. Each detected trend center is pushed into the model template $\mathcal{M}$, used for spatial consistency check.
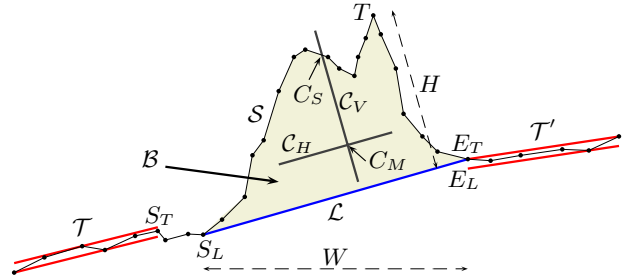

Figure 4. Bump model construction.

The construction of the bump model (see Figure 4) is as follows: let $\mathcal{L}$ be the baseline of the convex hull of the profile point subsequence between trend end points S_T and E_T. In lack of detected trends, the whole sequence $\mathcal{P}$ is considered. More precisely, this baseline is the convex hull segment $S_L E_L$ below the highest point T in the subsequence. Let $\mathcal{S}$ be the polyline joining the profile points from S_L to E_L, and $\mathcal{B}$ be the polygon closed by $\mathcal{L}$ and $\mathcal{S}$. $\mathcal{C}_V$ (resp. $\mathcal{C}_H$) is the orthogonal (resp. parallel) line to baseline $\mathcal{L}$ splitting $\mathcal{B}$ in two parts of equal area. The bump center of mass C_M is the intersection of $\mathcal{C}_V$ and $\mathcal{C}_H$, and the bump surface center C_S the intersection of $\mathcal{C}_V$ and $\mathcal{S}$. In this new bump model, it is left possible to select either C_M or C_S to define the bump center C. The bump width W is defined as the horizontal length of the baseline, and the bump height H as the distance of the bump summit T to the

baseline. Center C, width W and height H values are pushed in the template $\mathcal{M}$ used for checking consistency in the detection framework. Center selection allows to consider only the volume (with C_M) or also the surface (with C_S) when ensuring spatial consistency. A hollow structure is obtained on the same principle by symmetry around the baseline.

Trends are detected before the bump construction because they contribute to get much better localized baseline end points S_L and E_L. The bump (polygon $\mathcal{B}$) area can then be more reliably estimated. But in many areas, the surface is largely perturbated so that trends cannot be detected. For instance, a tree windthrow may cause such perturbation. The bump can anyway be constructed, but it is not labelled as reliable. Knowing the distance between successive scans, it is then possible to get an interpolated estimation of the ridge volume between two reliable bumps. Trend detection adds additional constraints into the structure extraction process, so that output structures are generally much shorter. Therefore it is left as an option.

3.3 ILSD implementation

For larger accessibility and improved reusability, the development is based on light easily integrated cross-platform libraries: GLFW[1] to handle windows and render context, Glad[2] to load OpenGL 3D tools on Windows (GLEW[3] on Mac OS), ImGui[4] for the user interface, STB[5] for image format handling, and ShapeLib[6] to export detected structures in shape format accepted by most GIS. Sources and executable code of ILSD are available in a public *GitHub* repository: https://github.com/evenp/ILSD.git.

4. THE LIDAR ACQUISITION

The archaeological prospections took place in the Fossard mountain (see Figure 5) in western part of the vosgian massif (France). This area is covered by a forest vegetation, with a large ratio of conifer plantations. A LiDAR acquisition campaign was realized in December 2018, covering a much wider sector, using a Titan DW device. Flight speed was 58 m/s, at 1150 m height for a slope ranging from 400 m up to 800 m. The scan angle was set to $\pm 21^o$ to ensure a 50% swath overlap. The acquired data were parted in 500×500 m^2 tiles, each containing a set of classified points stored in LAZ format (compressed version of ASPRS laser file) and a 1000×1000 pixels resolution DTM.
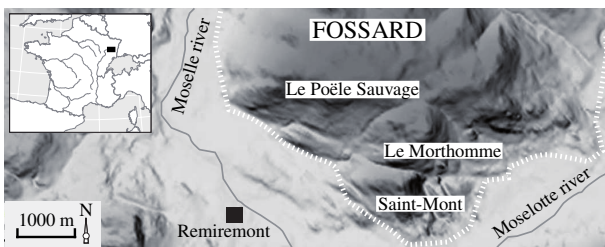

Figure 5. Map of tested area.

[1] https://github.com/glfw/glfw.git
[2] https://glad.dav1d.de
[3] https://github.com/nigels-com/glew.git
[4] https://github.com/ocornut/imgui.git
[5] https://github.com/nothings/stb.git
[6] https://github.com/OSGeo/shapelib

Despite a mean density of 9.7 ground points / m^2 in used tiles, quite large variations occur all over Saint-Mont sector and its vicinity. Most occluded places are due to a large amount of evergreen vegetation areas. This irregular point cover strengthens the choice of a detection tool based on raw data analysis, more aware of holes in the ground point cloud.

5. ARCHAEOLOGICAL RIDGE STRUCTURES

5.1 Presentation of the site

The Saint-Mont (see Figure 5) is a promontary in the south of the Fossard, with very rich archaeological and historical past. Established on a ruined castrum, a monasterium, associated to a funeral enclosure, was founded on its summit in the 7th century, and occupied until the 18th century (Kraemer, Chenal, 2018). Linked to the monastery, the castrum, or to potential late Antiquity (5th c.) occupations, several monumental dry stone walls inscribed in the landscape could correspond to a defense system which blocks the acces to the summit (Grzesznik, 2020).
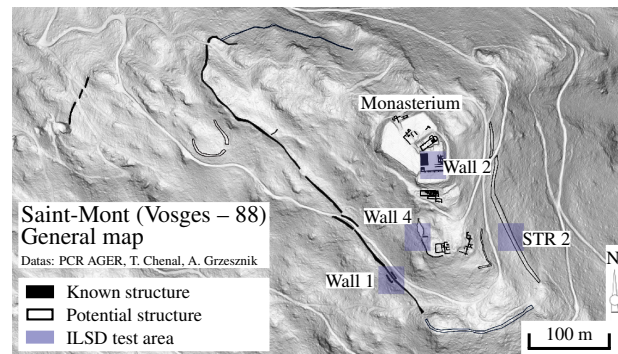

Figure 6. Archaeological prospections on St Mont.

These linear structures, akin to destroyed or partially destroyed walls on the slopes, form three enclosures (see Figure 6).

The Saint-Mont mountain has a complex topography. In the eastern part of the studied area, it is characterized by its stiff slopes, where screes of several thousand square meters extend. This area is not easily accessible with cliffs preventing any passage in its lower part, and only some secondary paths cross it. To the west, the extensive slope, articulated with many platforms, is more reachable than east and south ones. Here also, the field is rugged with many screes. The northern steep valley appears as a defensive link between western and eastern slopes. Studying this system makes it possible to explore the management of space and landscape during past time periods, known or not. One difficulty of this site deals with the complex mixture of natural (screes) and man-made similar structures (more or less decayed walls).

An interdisciplinary methodology has been implemented since 2012. Various field surveys accompanied by differential GPS point-taking have made it possible to draw up a more precise mapping of the geographical distribution and topographical implantation of the walls. Then, a topographic survey of the entire western slope was realized, in order to specify these various parameters. A series of archaeological surveys was also carried out on three enclosures (see Figure 6). Archaeological excavations explained how the structure was founded on natural screes or how far this last has been covered by a decayed part of the wall. These surveys were refined using the LiDAR acquisation.

The conventional DTM was essential in the visualization of the many structures arranged on the whole site, suggesting that the enclosure system could be more extensive than first expected.

5.2 Achieved results using ILSD

A dozen of structures were tested. Four were selected to illustrate this evaluation campaign. First, the tool was tested on well-known archaeological structures, whose linear shape and high visibility in the landscape allow semi-automatic detection to be tested. The tool was applied to two archaeologically documented walls (1 and 4). Concerning wall 1, although this well preserved structure is cut by a forest track and lays on a natural topographic accident, the tool easily detects 80 % of this wall in its best preserved section. This extends over 15 m wide, for a maximum height of 1.10 m. Well detected local trends on each side allows to measure the volume of the structure (415 m^3) on a 137 m long part. Displayed cross sections make it possible to accurately restore the morphology of the structure and its implantation environment (see Figure 7).
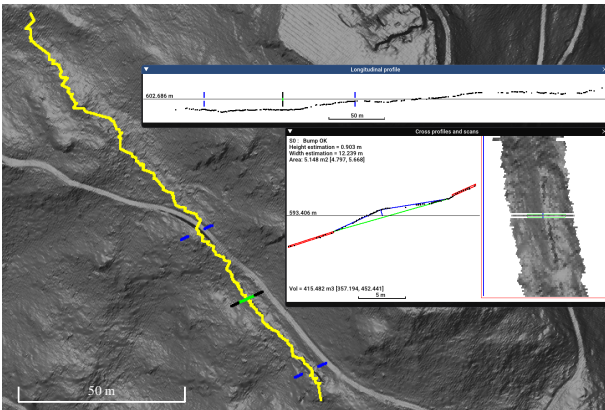

Figure 7. Detection and analysis of Wall 1 structure; local trends in red, detected bump in blue, baseline in green; blue strokes: measure bounds, green stroke: input trend.

This manipulation was repeated on the enclosure wall 4. The entire section is well detected. The tool takes into account the change in orientation of this less preserved structure. In addition, a possible continuation of this structure was displayed on a plausible layout according to terrain observations. Wall 2 structure is a masonry wall, particularly well studied, lying on St-Mont platform where the point density is the highest. Its detection required a careful parameter setting, due to its small dimension (0.4 m wide and 0.1 m high). Using the same parameters, excepted the ground point lack tolerance that had to be enlarged, the tool was able to immediately discover STR 2 structure crossing the southern slope in a dense forest sector, that could correspond to the extension of the main wall. ILSD allows here to follow its layout over 150 m, the cross section showing non natural break in the slope. This information will help to speed up the archaeological field surveys.

ILSD brought innovative perspectives to detect archaeological ridge structures. It allows the analysis of the lidar sparse point cloud, and avoids loosing time with interpolation errors inherent to classical conventional DTM.

Among preliminary cartographic spotting and other field survey, ILSD can also be used by archaeologists to prepare their fieldwork. ILSD stands out as an effective means to examine
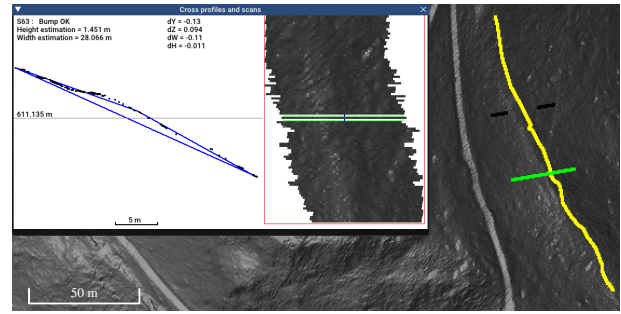

Figure 8. Detected layout of STR 2 structure.

landscape anomalies, by displaying cross sections of the structures from the point cloud. Furthermore, the semi-automatic detection makes it possible to highlight and measure potential structures, that could be long to detect using classical raster analysis tools. It is also particularly valuable in forested or mountainous landscapes where access and perception conditions are often degraded.

6. MAN-MADE HOLLOW STRUCTURES

6.1 Context

Sheet erosion is now well studied in Western Europe (Dreibrodt et al., 2010, Fechner et al., 2014) and revealed variation of rate due to intricated man (cultivation) / climate (rain) influence. Concentrate erosion is favored by holloways. Their role as source of water and sediment runoff is widely recognized (Boardman, 2013, Froehlich, 1991).

Holloways are sunken portions of tracks that have been used as well for long distance traffic of people, cattle or raw material, as for local exploitation of wood, charcoal or stones, mineral extraction, artisanal/industrial activities (iron melting, turf ...), or for military movements. On steep forested slopes for example, logs were traditionnaly carried off with the help of a sledge called *schlitte* which created an impressive downslope network of sunkentracks (Gebhardt, 2008). On the geomorphological point of view, holloways can be considered as gullies activated by man induced traffic. They are formed by increasing erosion at break-in-slope points on soft geological cover, as soon as the slope exceeds 2 to 4 % (Boardman, 2013, De Geeter et al., 2020).

Complementary to other aerial imagery, LiDAR can help to detect old holloways under forest cover, to determine main traffic orientation and to hierarchize the different tracks (traversing the whole sector, related to local sites settlement/exploitation, ...). In this last case it points out potential archaeological sites or ancient wood, stone or charcoal extraction plots. As sunkenlanes supply 60-70 % of the annual sediment erosion rate compared to holocene gullies (10-15 %), to surface sheetwash and to the very seldom water runoff under forest (1 %) (Froehlich, 1991), ILSD may provide a quick estimate of quantity of eroded sediment material on a hillside slope at a watershed scale. Comparing different hillsides may also open questions on the potential ancient anthropisation of a specific area.

Old tracks laying-out also results in the interaction between an anthropic need and natural constraints (cliffs, rocks, slope steepness, soil movements, linear water runoff, ...). Displaying the longitudinal profile of the structures and the surrounding

slope trend, a tool like ILSD can help to understand local sunkness of a lane or the cause of it local deviation.

Five different types of linear hollow structures (LHS) are selected on the studied area of the LiDAR map (see Figure 9):

A) simple linear hollow structures on a gentle slope,
B) intricated linear hollow structures,
C) simple hollow quarry tracks,
D) simple linear hollow structures on a steep slope,
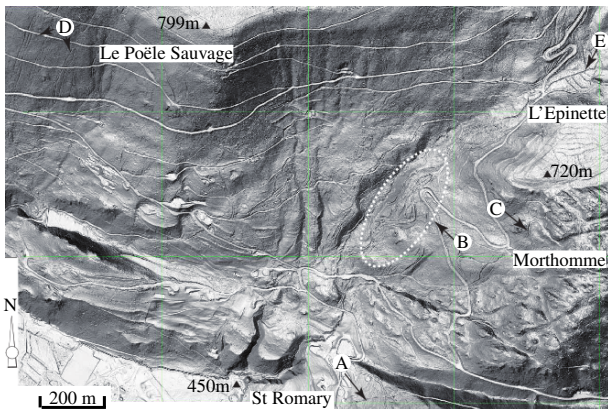E) modern mechanical drains for comparison.

Figure 9. Location of studied hollow structures.

The use of structures C and E is well-known and they provide a reference, while the origin of structures A, B and D is still not established.

6.2 Results

At first, several parameters were measured on the best detected linear hollow structures profile (see Table 1). The slope gradient is obtained from the height difference between the start and the end of the lane and its horizontal length (the length of the projected layout on a horizontal plane). The width and depth evolution of the structure indicates its shape/profile evolution. The volume suggests the estimated extracted/eroded volume of sediment on selected parts. Computed lower and upper bounds are also displayed in the table to provide an indication on its accuracy. A set of tests was realized on whole detected structures, unreliable end parts apart (refered as *total* in the table). In order to better compare the data, around 20 m long sections of the best preserved part of each linear hollow structure investigated were also analyzed.

On the simple hollow structure of gentle slope example A (see Figure 9, Table 1), we compared the total length, the upper part of the structure (see Figure 11, a, b, d), the lower part (see Figure 11, a, c) and the 20 m of best preserved hollow portion. The detected structure showed some local deviations (see Figure 10, I, II, III) where the tracking fails, although the ground point density is correct.

In cases I and II, the displayed cross profiles showed a local raising of hollow structure basement. This could not come from a less erosion in this regular gentle slope gradient. On site verification revealed anthropogenic perturbations. At spot I (see Figure 11, a, d), the ancient hollow structure (see Figure 11, b) was filled in again allowing recent crossing between two forest plots (see Figure 11, d). In the lower part (see Figure 11, a, II–III), the detection deviated to follow a large shallow carriage
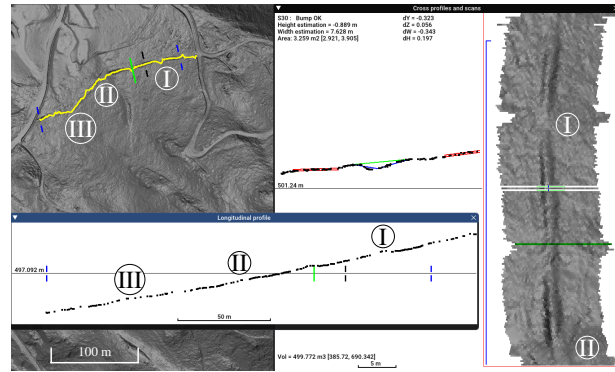

Figure 10. Analysis of a simple hollow structure. On left: main view with extracted structure on DTM shaded map; at center: bump model displayed over collected points of the selected cross profile (black); on right, processed scans centered on input stroke (green); at bottom: longitudinal point profile with measured area bounds (blue).

track coming from a now forested ancient stoned meadow or pasture (see Figure 11 c, II–III), and joined again the old hollow track before it is cut by the actual road. Measurements of this gentle slope gradient (see Table 1, A, LHS 04 and 05) indicates that the volume of missing sediment in the upper part of the track (170 m^3) compared to the shallower low section (143 m^3) can be related to a small slope gradient decrease between the two parts (19 against 17 %). But this observation may be tempered in regard to the lower amount of accepted bumps in the lower part, that reveals a more diffuse structure.
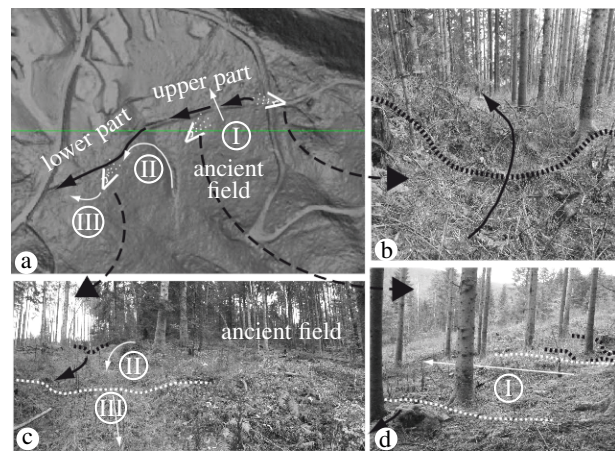

Figure 11. Simple hollow structure. ⇗: axis of views b, c, d; white arrow: recent track layout; black arrow: old track layout; white dots: recent track; black dots: old track.

The quarry example (see Table 1, C, LHS 21 to 23), shows less erosion in the steeper upper part of the slope (LHS 23, 72 m^3, 22 %) than in the lower part (LHS 22, 120 m^3, 18 %). This stronger erosion can be explained by more passage in LHS22 used for both quarries.

On steep slope example (see Table 1, D, LHS 11 31 to 35), a series of simple linear holloways shows more homogeneous erosion volume (58 to 62 m^3 for a length of 20 m). This is consistent with the constant slope gradient (54 %) noticed. These shallow structures (see Figure 12, b) are more difficult to detect and the ratio of reliable cross sections extracted is much lower than in other examples. This could point out short and discontinuous use of the structures over the time.

LHS	A^+ A^-	L (m)	SG (%)	W (m)	H (m)	V (m^3)	N_b N_a
A – Simple hollow structures							
02 (total)	513 476	212	18.1	3.65 ±1.27	0.87 ±0.32	499 385–690	343 173
03 ($\simeq$20 m)	498 494	22	18.6	3.55 ±0.96	1.17 ±0.34	50 43–56	40 34
04 (upper)	512 494	95	19.2	3.28 ±0.73	0.95 ±0.32	171 135–204	162 103
05 (lower)	492 480	67	16.9	4.26 ±1.67	0.83 ±0.27	143 94–164	103 41
B – Intricated hollow structures							
11 (total)	607 594	81	16.9	5.67 ±1.41	2.05 ±0.45	557 475–634	125 55
12 ($\simeq$20 m)	603 599	25	14.6	5.81 ±2.05	2.44 ±0.36	226 202–275	40 14
14 (total)	627 621	52	12.0	4.66 ±1.17	1.27 ±0.26	221 178–246	90 37
15 ($\simeq$20 m)	626 623	26	11.4	4.58 ±1.01	1.36 ±0.23	120 98–125	44 17
C – Simple old quarry tracks							
21 (total)	681 662	102	19.5	4.90 ±1.51	1.09 ±0.30	479 430–518	187 55
22 ($\simeq$20 m)	681 677	24	18.7	4.60 ±0.37	1.49 ±0.29	120 110–128	42 12
23 ($\simeq$20 m)	692 688	21	21.9	5.31 ±2.57	0.82 ±0.15	72 63–79	41 7
D – Simple linear hollow structures on steep slope							
32 (total)	656 625	68	52.8	2.99 ±1.01	0.71 ±0.17	153 113–192	113 11
33 ($\simeq$20 m)	636 625	25	54.5	2.91 ±0.75	0.73 ±0.19	58 41–76	39 8
34 (total)	642 604	86	51.1	2.77 ±0.83	0.89 ±0.25	183 127–230	152 24
35 ($\simeq$20 m)	635 624	23	53.8	3.18 ±0.72	1.12 ±0.13	63 49–74	41 9
E – Mechanical drains							
41 (total)	707 705	67	2.8	3.07 ±0.93	0.90 ±0.17	110 80–123	149 44
42 ($\simeq$20 m)	706 705	17	3.5	2.95 ±0.74	0.83 ±0.12	30 25–36	40 19

Table 1. Linear hollow structures measures.
A: altitude, L: 3D length, SG: slope gradient, W: mean width, H: mean depth, V: volume, N_b: number of selected bumps, N_a: number of accepted bumps.

The drain example (see Table 1, E, LHS 41 to 42), used for validation, corresponds to drainage works to sweeten the soil before planting fir trees. Along 20 m, it shows a very little slope (3 %) for an extracted volume of about 30 m³. Found measures (LHS 42, 30 m³, 3 %) are consistent with what was expected for structures dug by mechanical engines on rather flat area, with no noticeable water erosion afterwards.

In the intricated structures example (see Table 1, B, LHS 11 to 15), important sediment loss can be observed in regard of the slope gradient (for instance, LHS 12, 226 m³, 15 %). This denotes stronger erosion, probably due to intensive use compared to the steep slope structures. In this sector, the terrain is very perturbated (see Figure 12, a) and makes it quite difficult to obtain reliable trends to ensure correct measurements. However many of these sharp structures can be extracted if trend detection is discarded, despite of lower ground point density in this close wood area. Without trends, a volume estimation could be obtained, but at the price of heavy manual settings of each

Figure 12. Comparative views of: a) shallow structures on steep slope; b) intricated deep structures.

bump baseline.

The detection of hollow linear structures using the semi-automatic tool ILSD quickly brought a sufficient data set to understand their geometry (length, depth, width, volume, curvilinear slope profile). The obtained average volume of missing sediment can be exploited by geomorphologists for erosion calculation at a watershed scale. This also may help to easily highlight anomalies in a holloway network organization, that may be useful in the frame of research on past use evolution of a local landscape.

7. CONCLUSION AND PERSPECTIVES

This paper introduced an interactive tool, called ILSD, to extract linear ridge and hollow structures from LiDAR raw data and immediately visualize and measure their cross and longitudinal profiles. Processing raw data rather than the interpolated DTM makes it aware of irregular point repartitions due to LiDAR signal occlusion by a dense vegetation cover. This may contribute to reduce the risk of misinterpretation caused by the heterogeneous ground point arrangement, especially in forested environments. Based on a recent curvilinear structure extraction framework using efficient digital geometry algorithms, fast execution time achieved ensures a good level of interaction to extract several hundreds of meters long structures. The original ridge model was enriched with the detection of surrounding local trend to provide more accurate bounds to localize the structure and allow geometrical properties estimations.

The tool was tested in real situations by archaeologists to evaluate the efficiency and the potential interest of this approach. To that end, a multi-platform prototype based on open access libraries was realized and is still left available to future potential users. Despite a complex user interface with different parameters to set, many extractions could be rapidly achieved and used to collect valuable data. Tests realized on already well-studied enclosure walls showed that metric information can be easily collected, whereas this work takes much longer time using classical raster analysis tools on GIS. Possible layouts for unknown structures can also be quickly checked and displayed, thus allowing to speed up terrain prospections. Besides, the tool was used in the scope of a prospective research work on the impact of man on its environment, to extract and characterize hollow structures. Rough metric estimates of eroded volumes or slope gradient of the longitudinal profile could efficiently be obtained for most tested holloways, when regular terrain trends can be detected on both sides.

The digital geometry tools used in this work are intrinsically subject to large direction changes in the structure layout. This could be solved by integrating signal processing techniques to predict these events and allow longer structure extension in relevant direction. In the same vein, the estimated measures could be made more accurate using filtering techniques. In particular,

the fluctuations of the bump center positions produce a hectic behavior of the structure layout and an overestimation of its curvilinear length. In that sense, the on-line code is certainly far from perfect, but we hope that in a near future, its availability will facilitate the integration of the linear structure extraction function into GIS softwares to let larger access to the promising facilities disclosed by achieved experiments. At longer term, a possible extension of this work is the development of automatic solutions to detect some specific structures using convolutional neural networks. To that end, ILSD could be used to facilitate data annotation tasks in order to provide the required learning basis.

REFERENCES

Amable, G., Devereux, B., Cockerell, T., Renshaw, G., 2004. Analysis of interaction patterns between vegetation canopies and small footprint, high-density, airborne LIDAR. *The International Archives of the Photogrammetry, Remote Sensing and Spatial Information Sciences*, 34(B7), 1085–1089.

Axelsson, P., 2000. DEM generation from laser scanner data using adaptive TIN models. *International Archives of Photogrammetry and Remote Sensing*, XXXIII(part B4/1), 110–117.

Bennett, R., Welham, K., Hill, R. A., Ford, A., 2012. A comparison of visualization techniques for models created from airborne laser scanned data. *Archaeological Prospection*, 19, 41–48. doi.org/10.1002/arp.1414.

Boardman, J., 2013. The hydrological role of 'sunken lanes' with respect to sediment mobilization and delivery to watercourses with particular reference to West Sussex, southern England. *Journal of Soils and Sediments*, 13(9), 1636–1644. doi.org/10.1007/s11368-013-0754-7.

Challis, K., Forlin, P., Kincey, M., 2011. A generic toolkit for the visualisation of archaeological features on airborne LiDAR elevation data. *Archaeological Prospection*, 18(4), 279–289. doi.org/10.1002/arp.421.

De Geeter, S., Poesen, J., Vanmaercke, M., 2020. Does the topographic threshold concept explain the initiation points of sunken lanes in the European loess belt? *Catena*, 192. doi.org/10.1016/j.catena.2020.104586.

Devereux, B., Amable, G., Crow, P., Cliff, A., 2005. The potential of airborne lidar for detection of archaeological features under woodland canopies. *Antiquity*, 79, 648–660. doi.org/10.1017/S0003598X00114589.

Doneus, M., Briese, C., Fera, M., Janner, M., 2008. Archaeological prospection of forested areas using full-waveform airborne laser scanning. *Journal of Archaeological Science*, 35, 882–893. doi.org/10.1016/j.jas.2007.06.013.

Dreibrodt, S., Lubos, C., Terhorst, B., Damm, B., Bork, H.-R., 2010. Historical soil erosion by water in Germany: Scales and archives, chronology, research perspectives. *Quaternary International*, 222, 80–95. doi.org/10.1016/j.quaint.2009.06.014.

Even, P., Ngo, P., 2020. Live extraction of curvilinear structures from LiDAR raw data. *ISPRS Annals of the Photogrammetry, Remote Sensing and Spatial Information Sciences (XXIV ISPRS Congress)*, V-2, 211–219. doi.org/10.5194/isprs-annals-V-2-2020-211-2020.

Fechner, K., Baes, R., Louwagie, G., Gebhardt, A., 2014. Relic holocene colluvial and alluvial depositions in the basins of the Scheldt, the Meuse, the Somme, the Seine and the Rhine (Belgium, Luxemburg and Northern France). *The archaeology of erosion, the erosion of archaeology*, Relicta (Monogrefieën), Flanders Heritage Agency, Brussels, 147–190.

Froehlich, W., 1991. Sediment production from unmetalled road surfaces. *Sediment and Stream Water Quality in a Changing Environment*, 203, 21–29.

Gebhardt, A., 2008. Impacts anthropiques anciens sur les sols forestiers. quelques études de cas en contexte archéologique et expérimental. J.-L. Dupouey, E. Dambrine, C. Dardignac, M. George-Leroy (eds), *Sylva, la mémoire des forêts*, 211–218.

Georges-Leroy, M., Bock, J., Dambrine, E., Dupouey, J.-L., 2011. Contribution of lidar data to the study of land-use history in Haye forest. *ArcheoSciences*, 35, 117–129. doi.org/10.4000/archeosciences.3015.

Grzesznik, A., 2020. Le Saint-Mont : système d'enceintes en pierre sèche. Rapport de prospection thématique et de sondages, Service Régional de l'Archéologie, Metz.

Jiang, X., Bunke, H., 1994. Fast segmentation of range images into planar regions by scan line grouping. *Machine Vision and Applications*, 7, 115–122. doi.org/10.1007/BF01215806.

Jones, A. F., Brewer, P. A., Johnstone, E., Macklin, M. G., 2007. High-resolution interpretative geomorphological mapping of river valley environments using airborne LiDAR data. *Earth Surface Processes and Landforms*, 32, 1574–1592. doi.org/10.1002/esp.1505.

Kraemer, C., Chenal, T., 2018. D'Amé et Macteflède à Imma, approche topographique du monastère féminin du Romarici mons, entre le VII e et le IX e siècle. *Colomban et son influence. Moines et monastères du Haut Moyen-Âge en Europe (actes du colloque de Luxeuil-les-Bains)*, Presses Universitaires de Rennes, 331–352.

Lasaponara, R., Coluzzi, R., Masini, N., 2011. Flights into the past: full-waveform airborne laser scanning data for archaeological investigation. *Journal of Archaeological Science*, 38(9), 2061–2070. doi.org/10.1016/j.jas.2010.10.003.

Mallet, C., Bretar, F., 2009. Full-waveform topographic Lidar: state-of-the-art. *ISPRS Journal of Photogrammetry and Remote Sensing*, 64(1), 1–16. doi.org/10.1016/j.isprsjprs.2008.09.007.

Mayoral, A., Toumazet, J.-P., Simon, F.-X., Vautier, F., Peiry, J.-L., 2017. The highest gradient model: a new method for analytical assessment of the efficiency of LiDAR-derived visualization techniques for landform detection and mapping. *Remote Sensing*, 9(2). doi.org/10.3390/rs9020120.

Popescu, S. C., Wynne, R. H., Nelson, R. F., 2002. Estimating plot-level tree heights with lidar: local filtering with a canopy-height based variable window size. *Computers and Electronics in Agriculture*, 37(1-3), 71–95. doi.org/10.1016/S0168-1699(02)00121-7.

Sevara, C., Pregesbauer, M., Doneus, M., Verhoeven, G., Trinks, I., 2016. Pixel versus object – a comparison of strategies for the semi-automated mapping of archaeological features using airborne laser scanning data. *Journal of Archaeological Science: Reports*, 5, 485–498. doi.org/10.1016/j.jasrep.2015.12.023.

Sithole, G., Vosselman, G., 2006. Bridge detection in airborne laser scanner data. *ISPRS Journal of Photogrammetry & Remote Sensing*, 61, 33–46. doi.org/10.1016/j.isprsjprs.2006.07.004.

Sittler, B., 2004. Revealing historical landscapes by using airborne laser scanning. A 3-D model of ridge and furrow in forests near Rastatt (Germany). *International Archives of Photogrammetry and Remote Sensing*, XXXVI(Part 8/W2), 258–261.

Štular, B., Kokalj, Ž., Oštir, K., Nuninger, L., 2012. Visualization of lidar-derived relief models for detection of archaeological features. *Journal of Archaeological Science*, 39(11), 3354–3360. doi.org/10.1002/arp.374.

Toumazet, J.-P., Vautier, F., Roussel, E., Dousteyssier, B., 2017. Automatic detection of complex archaeological grazing structures using airborne laser scanning data. *Journal of Archaeological Science: Reports*, 12, 569–579. doi.org/10.1016/j.jasrep.2017.03.012.

Trier, Ø. D., Salberg, A.-B., Pilø, L. H., 2016. Semi-automatic mapping of charcoal kilns from airborne laser scanning data using deep learning. *Oceans of Data: Proc. of the 44th Conference on Computer Applications and Quantitative Methods in Archaeology*, 219–231.

Trier, Ø. D., Zortea, M., Tonning, C., 2015. Automatic detection of mound structures in airborne laser scanning data. *Journal of Archaeological Science: Reports*, 2, 69–79. doi.org/10.1016/j.jasrep.2015.01.005.

Wehr, A., Lohr, U., 1999. Airborne laser scanning – an introduction and overview. *ISPRS Journal of Photogrammetry and Remote Sensing*, 54(2–3), 68–82. doi.org/10.1016/S0924-2716(99)00011-8.

Wu, T., Hu, X., Ye, L., 2016. Fast and accurate plane segmentation of airborne LiDAR point cloud using cross-line elements. *Remote Sensing*, 8(5). doi.org/10.3390/rs8050383.